IMAGING THE IONOSPHERE WITH THE GLOBAL POSITIONING SYSTEM

George A. Hajj, R. Ibanez-Meier, and E. R. Kursinski

Jet Propulsion Laboratory

California Institute of Technology

ABSTRACT

Observing the Global Positioning System by a satellite in Low earth orbit in an occulting geometry provides a powerful means of imaging the ionosphere. Tomographic imaging of the ionosphere is examined using singular value decomposition analysis. The interdependency of the obtainable resolution, the accuracy of the solution and the data noise is explained. A simulation is done where a 2-D ionospheric structure is generated. Accuracy of imaging the ionosphere using ground and/or flight data is examined. The GPS occultation data show sensitivity to the E layer

1. INTRODUCTION

When a radio wave travels through the ionosphere, it experiences a group delay or a phase advance that is, to first order, proportional to the total electron content between the transmitter and the receiver [1]. The total electron content is defined as the line integral of the ionospheric free electron density between the transmitter and the receiver. Measurements of TEC have been achieved by different techniques with different degrees of accuracy and precision; all of these techniques involve a radio beacon satellite and a receiver. With an array of receivers tracking the same or different satellites, it is possible to obtain a set of intersecting links with a TEC measurement for each link. In such case we have a situation similar to that of X-ray projections in medical imaging where the image can be obtained using inversion methods.

Unlike medical imaging however, in ionospheric imaging the geometry of the intersecting links can be quite arbitrary and therefore in many situations it lacks the sufficient strength to provide a unique inversion. In this case one can only reconstruct a solution which contains characteristics that the data are able to resolve.

The possibility of doing 2-D ionospheric tomography has been considered by many authors [2-10]. Work by Raymund et. al. [4,10] and Yeh and Raymund [6] showed the limitation of ionospheric tomography as obtained from ground data alone. This is due to the lack of links that cross the ionosphere in a tangential geometry. These links can only be provided by a transmitter and a receiver in space viewing each other in an occultation geometry. In a radio occultation geometry, a transmitting satellite is setting or rising behind the earth's atmosphere as seen by a receiver in space. This is possible through use of signals transmitted by satellites of the Global Positioning System (GPS) and received by one or more other satellites in Low Earth-Orbit (LEO) (Fig.). As the signal passes through the ionosphere, its phase speeds up and bends, in accordance with Snell's law, as a result of the changing index of refraction at different heights of the ionosphere. This bending translates into a doppler shift which is over and above the doppler due to the motion of the spacecrafts. This measured extra doppler can be translated into an estimate of the total bending of the signal, α, as a function of the asymptote ray distance, a (Fig. 1). Once $\alpha(a)$ is determined, and assuming the ionosphere to be spherically symmetric in the region where the occultation is taking place, then the atmospheric index of refraction is obtained by an Abel transform of $\alpha(a)$ Radio occultation techniques have a heritage of over 20 years in NASA's planetary program, but the concept is a newcomer into the earth science arena and can be applied to both the neutral atmosphere and the ionosphere 8]

An alternative approach to using the doppler shift is to ignore the bending induced by the ionosphere (bending on the day side is of the order of 0.01 degrees. Ignoring bending is certainly valid as a first approximation) and assume the signal to be going through a straight line. Then with a simple linear combination of the dual L-band frequencies of the GPS, one can find the

total electron content along the straight line between the GPS and LEO satellites. Using an onion-shell model for the ionosphere, one can solve for the index of refraction at different layers as the tangent point (closest approach point in the link to the center of the earth, see Fig. 1) starts at the top of the ionosphere and descends into deeper layers of the atmosphere. With a satellite at 800 km altitude, the ray descends (ascends) for a setting (rising) GPS at a speed of 3 km/s. This implies that it takes less than 5 minutes to sample the ionosphere in the occultation region.

The GPS consists of 24 satellites, evenly distributed in 6 orbital planes around the globe with an inclination of ~55°, at about 20200 km altitude and a revolution period of 12 hours (Fig. 2). Each satellite transmits two carrier frequencies at L-band, L1 and L2 at 19.0 cm an 24.4 cm respectively. The carrier signals are modulated by a pseudo-random code which allows measuring the absolute time delay between a GPS transmitter and a receiver [19]. This absolute time delay includes travel time between the transmitter and the receiver, effect of the medium which may include the ionosphere and the neutral atmosphere depending on the location of the receiver, and clock biases of transmitter and receiver in addition to noise. It has been demonstrated that clock biases can be solved to the nanosecond level accuracies [20]; this implies that absolute TEC measurements from GPS can be obtained with an accuracy of a few TEC units (1 TEC unit = 10^{16} e/m^2). On the other hand, with a high performance GPS receiver, TEC changes obtained directly from the carrier phase measurements have an accuracy of 0.001 TEC units.

While the GPS was designed and funded by the US Air Force mainly for the purpose of navigation, the civilian community has taken advantage of its presence for a host of other applications. These include seismic tectonic motions [21], earth orientation and polar motion studies [22-23], gravimetry [24], atmospheric water vapor and ionospheric calibration [25-26] and ionospheric monitoring [27]. Atmospheric occultation is yet another very important application of the GPS in the areas of climate and weather monitoring [14-18] and ionospheric imaging. The idea of using the GPS for the purpose of ionospheric tomography was first

suggested by Yunck et. al. [28]. Since then, several studies have been conducted in this area [?9-31].

In this paper, we examine ways by which a LEO satellite tracking GPS can be used to image the ionosphere. Two problems are being discussed. One is to combine the LEO-GPS links with TEC data from the ground in a tomographic approach. The other is to use the LEO-GPS occultation geometry to obtain high resolution vertical profiles of the ionosphere. In order to address the former problem, we work out a 2-D example which will serve in defining the tomography problem and answering basic questions such as the expected resolution and accuracy as a function of the geometry of the transmitting and receiving elements as well as data noise. This is discussed in section 2. We also work out a realistic simulation whereby a 2-D image is reconstructed tomographically using ground data with and without LEO-GPS links; this is discussed in section 3. In section 4 the effect of the ionosphere on the occulting signal is examined in more details and means of obtaining high resolution vertical profiles of the ionosphere are presented. A conclusion are given in section 5.

2. PEDAGOGICAL EXAMPLE

Consider the geometry of Fig. 3, where we divide our region of interest which corresponds to a rectangle of **30()()x45()** km^2 into 20X?() pixels. Consider a transmitting satellite to be passing above this region, and three receivers located on the ground below this region as shown in the Fig. 3. The corresponding links between the transmitter and the receiver are also shown. Only measurements as low as 13° elevation from the side receivers and 20° elevation from the middle receiver are included in our data set, This is to guarantee that there is no extra contribution to the TEC from outside the region of itll(.lest. We also assume that the free electron density is negligible above this region so that TEC measurements are due only to the electron density that lies mostly within the region of interest. This assumption is not generally valid since the ionosphere extends well above]()()() Km, but this example will illustrate the dependence of the solution on several factors such as the geometry of the links and the choice of a particular

basis to span the solution (in this example our basis is a set of pixels) This example is valid however, if the transmitting satellite is at a height comparable to 450 km. We number our pixels from -400, with 1 being the pixel in the lower left corner as shown in the Fig. 3.

Let the electron density function be denoted by $f(\underset{\sim}{r})$ where $\underset{\sim}{r}$ is a vector from a suitable origin to a given point in the image. A TEC measurement is then given by

$$C_j = \int_{RAYPATH\,j} f(\underset{\sim}{r})\, d\underset{\sim}{s}\ ; \quad j = \ , no.\ of\ links \qquad ($$

where $d\underset{\sim}{s}$ is an increment along a specific link j. We choose the following basis to span our solution

$$f_i(\underset{\sim}{r}) = 1 \text{ if } \underset{\sim}{r} \in \text{ pixel } i; \\ = 0 \text{ otherwise} \qquad (2)$$

We approximate $f(\underset{\sim}{r})$ by its digitized function, $f_d(\underset{\sim}{r})$, which is defined by

$$f_d(\underset{\sim}{r}) = \sum_{i=1}^{400} x_i f_i(\underset{\sim}{r}), \qquad (3)$$

where x_i is the a of $f(\underset{\sim}{r})$ in the ith pixel. Eq (can then be written in a matrix form as

$$\underset{mx1}{C} = \underset{mxn}{D}\ \underset{nx1}{X} + \underset{mx}{E}\ , \qquad (4$$

where C is a column of m measurements, X is a column of n unknowns, E is a column representing erro due to data noise and discretization, D is a m x n matrix with d_{ji} being the length of link j that lies in pixel i. Each element of E, denoted by o_j, is a function of two errors, the noise in measurement j, and the difference between the actual measurement and the one obtained from the discrete image Given the high precision measurements of TEC that can be obtained with the GPS system, o_j is dominated by the latter of these two errors. Furthermore the error introduced by discretization is also a function of the size of the pixel and the variability

of' the medium itself. Therefore σ_j will be larger for bigger pixels and for more variability in the medium. in what follows, we assume $\sigma_j = \sigma$ for all j's, The importance of determining σ will become evident below.

It is important to notice that in the example of Fig. 3, some pixels do not have any links passing through them. These elements in X and their corresponding null columns in D have to be removed from Eq. (4) at the outset before any inversion process is attempted. Once we do that for the example of Fig. 3, we end up with n= **392** unknown parameters. On the other hand we have m= **476** measurements.

Generally, D will not be of full rank; namely, only $L < m$ equations exist that are linearly independent. Moreover, the number of independent equations $L < n$, the number of unknowns. Therefore, we have an underdetermined system of equations. Singular value decomposition (SVD) of the matrix D allows us to remove the linearly dependent equations from our set of equations. Performing the SVD we write

$$\underset{m \times n}{D} = \underset{m \times L}{U} \; \underset{L \times L}{W} \; \underset{L \times n}{V^T} \tag{5}$$

where W is a diagonal $L \times L$ matrix with its diagonal elements equal to $(w_1, w_2, \ldots, w_L)$, sorted from 1-L in a decreasing order, which correspond to the non-zero singular eigen-values of D. The columns of U and V are the corresponding left and right singular eigen-vectors respectively. This factorization allows us to break the parameter space of X into two vector spaces. The first is the one spanned by the columns of $V = (v_1, v_2, \ldots, v_L)$. Each of these vectors corresponds to a linear combination of the original parameter space which can be solved for, with a variance given by

$$\sigma_i^{*2} = \frac{\sigma^2}{w_i^2} \tag{6}$$

The second region corresponds to the null space which is the part of the parameter space to which our data are not sensitive.

The singular values (SV) of our example is shown in Fig. 4. The following observations are to be made: The first 340 singular values (SV) decline by three orders of magnitudes. A sharp cutoff appears beyond the 340th singular value. The largest singular value w_1 corresponds to the best determined linear combination of the parameter space, namely the product $v_1^T \cdot X$. The second singular value w_2 corresponds to the second best determined linear combination of the parameter space, and so on. The geometrical interpretation of the eigenvectors v_i is that the first vector v_1 is the one that is most nearly parallel to the rows of D; therefore, it is the most nearly parallel to the direction of our links. The second vector is the one that is most nearly parallel to the remainder, etc. [32]

The least square solution for the system is given by

$$X = V \; W^{-1} U^T C \tag{7}$$

and the solution covariance by

$$cov(X) = \sigma^2 V W^{-2} V^T \tag{8}$$

The solution given in Eq. (7) is undetermined up to an arbitrary linear combination of the vectors spanning the null space. By not including any of these vectors, we are choosing the least norm solution among all other possible solutions. In the presence of some apriori knowledge about the ionosphere, one would set up the problem in exactly the same way as above. However,

X would correspond to the deviation from the apriori values for the electron density in each pixel, and C would be the difference between the measured value and the one calculated based on the apriori.

A fundamental issue remains which is choosing the number of non-zero singular values, w_i, to include in our solution. It is important to note from Eq. (7) that the more singular values we include in the solution, the closer we get to the true solution. On the other hand, including more and therefore smaller singular values causes the solution covariance to grow very rapidly as seen from Eq. (8). Different methods have been applied in choosing a cutoff value for the number of singular values to include [32]. The main point behind most of these methods is to choose a cutoff, I_C, such that the variance associated with the corresponding eigenvector as given by Eq. (6) makes physical sense. For instance, in the example above, suppose we have the error in the TEC measurement $\sigma = 10^{10}$ (e/m^2). This error is due to data noise and discretization as explained earlier. Then a cutoff at 100 km would corresponds to 10^{11}(e/m^3) of uncertainty in the electron density according to Eq. (6). Given that the electron density to be recovered can be of the same order of magnitude or smaller, this implies that one should not try to include more singular values in the solution.

Fig. 5 shows the solution for a unit impulse function in pixel 270 (see Fig. 3) which corresponds to the 270th column of VV^T with 100 singular values included. The reconstructed image resembles a 2-D sine function with a peak value of .38 and a width comparable to the dimensions of the pixel in the horizontal and vertical directions.

In order to characterize the resolution of a solution, we define the resolution of pixel i in a specific dimension as the length of pixel i in that dimension over the height of the reconstructed impulse function of that pixel. With this definition we proceed to examine the solution in a given pixel but with different number of singular values included in the sum of Eq. (7). Fig. 6 shows the horizontal and vertical resolution versus the standard deviation for pixel 270. The number of SV's included in the solution is indicated on the figure at different points. Based on this figure, if $\sigma = 10^{16}$ e/m^2, then the uncertainty in electron density at pixel 270 is about 10^{16} e/m^3 for $I_C = 150$. The corresponding resolution is about 300 km in the horizontal and 45 km in the vertical dimensions.

The discussion] in this section is not restricted to a basis consisting, of pixels, but can be generalized to any finite set of functions that we choose to expand the solution. The main question to be answered is how well does our finite. basis span actual structures in the ionosphere since that is a major contributor to the size of σ. We feel that this point is so fundamental to understanding the inherent relationship between the image, the basis in which we expand our solution, the data noise and the strength of data to recover the image where further elaboration is merited.

Consider the simple finite 2-1) image of the ionosphere shrew in Fig. 7 where the density is constant inside of each pixel. Furthermore, assume that our data is *noiseless*. ***Now*** consider that we scan the image from a specific angle, θ_1, such that our first link will only pass through a *single* pixel in the upper-rig,llt corner of the image. It is clew that the first link will immediately give the density in the first pixel. Su]qmsc.that we fix the viewing angle of our link but we move it in such a way that it crosses *one* additional new pixel at a time. Then each new data point will give the density of the additional new pixel that it passes through (Fig. 7). This process will allow us to reconstruct the densities in all the pixel from a single viewing angle of the image. A SVD analysis of links 1-4 yields four non-zero singular values. On the other hand a SVD analysis of links 5-8 gives only two non-zero singular values, since only two out of links 5-8 fire independent. in reality, if the picture is not discretized in exactly the same manner that we choose our pixels, links 1-4 will not be superior to links 5-8 but the SVD analysis is not capable of telling, us that directly. It is only through an independent estimate of σ, such as computing the post-fit residuals of the TEC data (difference between measured TEC and computed TEC based on the solution), that one. can compute the covariance of the solution and consequently estimate the strength of the data. Another important point to be made here is that if the basis functions chosen correspond to the correct modes of the image, then an accurate image can be obtained with a very restricted, but *appropriate*, set of data. This situation is demonstrated by Raymund c1 al. where a set of empirical orthonormal functions are used as a basis to capture large scale features of the ionosphere from a limited set of data [10, 33].

3. SIMULATION

We proceed by generating data based on a 2-1) slit.c of the ionosphere (Fig. 8). This 2-1) grid whit}) was generated according to the Parameterized Ionospheric Model (PIM) corresponds to the electron density at 20(" E geodetic longitude, 12:()() hr. universal time, September 26, 1992, and extends from -80° to +800" N geodetic lat it ude (only data from -200" to 400" N are shown in Fig. 8). The density is representative of the ionosphere during the day time, with a solar spot near solar maximum. PIM is a worldwide electron density profile model, developed by D. N. Anderson of the Air Force Phillips 1 .aboratory. This model is a parameterized version of the Utah State University model, which is a complete, first principles, ionospheric model using as inputs the solar UV flux wavelength profile, the Hedin neutral wind model, the MSIS-86 neutral atmosphere model, and an electric field model obtained from all available experimental data. The 2-D image has a main lobe at about 23° N latitude and 350 km altitude with a peak density of 2.3X 10^6(e/cm^3).

We limit our imaging to the region between -500" to 60° N. latitude and between 80 to 1000 km altitude. We divide this region into 22 pixels horizontally and ?2 pixels vertically. We place seven ground receivers at -200" -1 0°, (Y), 10°, 20°, 30° and 40° N latitude. Each receiver is tracking down to 10 degrees elevation with a data point taken every 2 degrees. Fig. 9.a shows the reconstruction of the region from ground data alone. The peak density of the reconstruction is about 1 .75x] 0^6 (e/cm^3) and is located at 20°-25° N latitude and 250 km altitude. The horizontal features such as the sharp gradient between] 0° N and 20° N and the maximum density between 1 5° N and 30° N are reflected in the reconstruction; however, a strong vertical correlation between the pixels is evident. The lack of the ground data alone to capture the vertical structure is due to the strong correlation of the ground data at all elevations with zenith measurements. This correlation makes the D matrix highly singular, and as explained earlier, only linear combinations of electron densities that are mostly parallel to the data links are we]] determined. The inability to capture vertical structures with ground data alone using

conventional tomographic methods or the convolution back projection algorithms is reflected in the literature [4, 34]. More recently, Raymund et d. [10] and Raymund [33] used the empirical orthonormal functions as a basis to capture the large scale structures of the ionosphere in both the horizontal and vertical directions. However, in this way, only features in the ionosphere that are truly represented by the empirical orthonormal set of functions can be recovered. Anti even then, only those functions that the ground data are sensitive to can be solved for, as discussed in the example of Fig. 7.

Fig. 9.b is the. reconstruction where the same data from ground is used in conjunction with a *single* occultation happening in the same 2-D plane with the tangent point of the occultations at] 0° N. In this case, we start to distinguish some of the more detailed features of the. 2-D structure, such as the high electron density near 20° N latitude and 300-400" km altitude. The slope of the main lobe. in the true image can, to some extent, be seen in the reconstruction. On the other hand, the tangential links have correlated the data in a way that made the sharp gradient at 15° N disappear. The maximum reconstructed electron density in this example is 1.9×10^6 e/cm^3.

In these two examples, the smallest cutoff included in the solution was equal to 100" km and no apriori was assumed. The fact that the solutions are of minimum norm explain why they underestimate the true density. Furthermore, no constraints were applied, which resulted in some negative electron densities (shown as purple pixels). The main point of these two examples is to see the effect of adding tangential links to ground data.

In real life situation, the fact that a GPS-LEO occultation may not fall in exactly the same plane as an array of ground receivers tracking some other low earth orbit satellite does not impose a real limitation. A genera] approach to using the GPS data would be to introduce profiles that can be accurately generated with the GPS at certain latitude-longitude points as constraints

or apriori to ground based solution. The topic of obtaining high resolution profiles with the GPS is discussed next.

4. IONOSPHERIC OCCULTATIONS

With the full constellation of the GPS satellites, a single GPS receiver in a near polar orbit will observe over 500 occultations per (lay, Spread about the globe. The first set of earth atmospheric occultations using GPS will be available when an 800 km altitude orbiter, GPS - MI :T, will be launched in May of 1994. GPS-MET will have a high precision receiver, capable of tracking 8 GPS satellites simultaneously. With an aft-looking ante.nna, the GPS-MET will cover only half of the full sky and therefore provide over 200" globally distributed occultations daily. A representative coverage of the. G} 'S-MET during one day is shown in 1 ig.10.

In the previous section, flight data has been used together with ground data mostly in the context of tomography where both horizontal and vertical resolution are being, solved for simultaneously. A second approach by which the f] ight data can be analyzed is by a direct inversion process of the bending angle $\alpha(a)$ (Fig. 1) via an Abe.] transform [1 1]. The theoretical limit of the vertical resolution obtainable through this technique is Set by the diffraction limit of the geometric optics approximation; namely, the vertical and the cmss-beam dimensions of the sampling, volume are approximatel y given by the diameter of the first Fresnel zone. in the absence of bending, the first Fresnel zone is approximately given by the diameter of a cone with its apex at the receiver, its axis being, the distance from the receiver to the tangent point, and the rays forming the cone having a length of this same distance plus one-half the radio wavelength. The Fresnel zone corresponds to about 1 km for a receiver in orbit at an altitude of 800" km observing a GPS satellite. However, a true limitation in reconstructing accurate ionospheric vertical profiles of electron density from occultation data alone is due to the relatively large horizontal structure that the signal ias to probe causing the spherical symmetry assumption to be inaccurate,. in what follows, wc will examine how well one can do by ig noring the horizontal gradient, and means of improving that.

We use our simulated structure of Fig.8 as the troth. in order to examine the effect of the ionosphere on the signal, we assume a geometry whereby a 1,1X) satellite is occulting a GPS satellite, with the tangent point of the occultation link at 20 deg. latitude. This latitude corresponds to the region of' maximum electron densit y profile in our 2-I) grid. The amount of bending and signal delay as a function of the height of the tangent point is shown in Fig.11 for the GPS 1.1 signal. The e ffect on the 1.2 signal is the. same but a factor of 1.65 bigger. The negative. delay implies a phase. advance. The curvature at a given point on the 1 .EO-GPS ray is in the direction of increasing index of refraction or decreasing electron density. (For the relationship between refractivity and electron density see reference 1.) A positive sig n of the bending angle is such that the curvature of the ray is toward the center of the earth. The bending of the ray is directly proportional to the amount of doppler shift that the ray experiences, which in turn is proportional to the phase change. This explains why the bending changes sign at the point where the delay is at a minimum near the F2 peak. The oscillations in bending near the E region arc similarly due to the change in curvature of the delay. It is worth noticing that even during the day time and near solar maxi mum, the absolute bending, does not exceed ().()16 (().()26) degrees for 1.1 (] .2). The magnitude of the delay for 1.1 is about 90 meters, which corresponds to a total electron content of about 250X] $()^{16}$ e/m^2.

Given that the bending]s small, in the following analysis we will assume that the signal travels along a straight path connecting the transmitter and the receiver. Assuming a locally spherically symmetric atmosphere, we solve for the electron density profiles for several occultations with tangent points at -20°, ()(), 200" and 40° N geodetic latitude. Fig. 1 2 shows the true electron density (solid line) and the reconstruction (open diamond) at these latitudes. The two peaks of each profile correspond to the F2 peak at 300-400 km altitude and the E peak at -1 ()() km altitude. The following observations will help in understanding some of the effect of the spherical symmetry assumption on the reconstruction.

The solution at 20° latitude largely underestimates the true profile. The reason being that the true electron density profile at about 200 corresponds to a maximum in the plane of occultation. This implies that the signal would be slower on bet]] sides of the. tangent point; therefore, on the average, it would give a smal ler estimate of the electron density. However, under general conditions, when the profile corresponds to neither a maximum nor a minimum with respect to its surrounding area, a cancellation effect take.s place and a more accurate reconstruction can be obtained. For instance, if for each layer that the signal is passing through, wc have a horizontal gradient that is changing lineally as a function of the arc length from the tangent point of occultation, the signal slows down and speeds up around the tangent point by exactly the same amount, so that the estimated refractivity is exactly that of the. tangent point. in the more general case, all odd components of the horizontal gradient around the tangent point cancel; only even terms contribute to the error in refractivit y [17]. This explains the almost exact agreement between the reconstructed and the. true profile above the F region for the. -200° latitude case where the actual electron density at that latitude is not exactly spherical. On the other hand, a sharp horizontal gradient in the electron density appears between 20° and 40° latitude and the gradient gets considerably smaller beyond 400° The net effect on the occultation with a tangent point at 400° is that the signal will travel faster on one side of the tangent point but not slow enough on the other side to compensate for the speed in the first side, resulting in an overestimate of the electron density.

Another problem of the reconstructed profile is that it depicts a negative electron density at the bottom of the ionosphere, which is a physical impossibility. imposing posit ivity on the solution can be used as an extra constraint to improve the results.

A first order improvement over the spherically symmetric assumption is to divide the ionosphere into pixels in the same manner that has been done'fm the tomography of section 3. Then constrain pixels lying next to each other horizontally (i.e. in the same layer) to have a given functional form with an undetermined scale factor. This functional form can be the same for all

layers, or different for different layers. Then one can solve for the unknown scale factor for each layer. This reduces a 2 or 3 dimensional problem into a one dimension problem where only the scale factor has to be found for each layer. Stated mathematically, this can be formulated as follow. Consider Eq. (4) where X is the column of n unknown densities corresponding to n pixels. Suppose. we have a 2-D image which is divided in polar coordinates into Θ slices in the angular direction and R layers radially as shown in Fig. 13. Let r_i be the radius of layer i and θ_j be the angle of the center of slice j. We correlate the elements of X as follow

$$
\begin{aligned}
x_1 &= \alpha_1\, g(r_1,\theta_1) \\
x_2 &= \alpha_1\, g(r_1,\theta_2) \\
&\\
x_\Theta &= \alpha_1\, g(r_1,\theta_\Theta) \\
x_{\Theta+1} &= \alpha_2\, g(r_2,\theta_1) \\
&\\
x_{2\Theta} &= \alpha_2\, g(r_2,\theta_\Theta) \\
x_{2\Theta+1} &= \alpha_3\, g(r_3,\theta_1) \\
&\cdot
\end{aligned}
\tag{9}
$$

where $\alpha_1, \alpha_2, \ldots, \alpha_R$ are unknown scaling, factors and $g(r,\theta)$ is a given function. Then Eq. (4) reduces to

$$
\underset{mx1}{C} = \underset{mxR}{B}\ \underset{Rx1}{A} + E \tag{10}
$$

where $A^T = (\alpha_1, \alpha_2, \ldots, \alpha_R)$ and the elements of B are given by

$$
\begin{aligned}
B_{1,1} &= d_{1,1}\, g(r_1,\theta_1) + d_{1,2}\, g(r_1,\theta_2) + \cdots + d_{1,\Theta}\, g(r_1,\theta_\Theta) \\
&\\
B_{1,2} &= d_{1,\Theta+1}\, g(r_2,\theta_1) + d_{1,\Theta+2}\, g(r_2,\theta_2) + \cdots + d_{1,2\Theta}\, g(r_2,\theta_\Theta)
\end{aligned}
\tag{11}
$$

d_{ij} are the original element of the matrix D in Eq. (4). By introducing the correlation function $g(r, \theta)$, the number of unknowns are reduced to R. in the case of an occultation, one can choose $m = R$ independent measurements and tile.rc.fore, obtain a unique solution for A^T.

Fig. 12 shows the reconstructed profiles when the same functional form is applied to ail the layers of the ionosphere, name.ly $g(r, \theta) = g(\theta)$. The applied function g(0) corresponds to the zenith total electron content from the ground up to 1000 km height at given latitude. Such data are generally available from models or global zenith '1'1 :C maps which are generated using GPS or by other means. *[26,30]* With the application of the same. horizontal gradient to correlate pixels at a given layer, the solution improves on average as seen from Fig. 12 (solid squares). A second order improvement is yet possible by applying ciiffc.rent horizontal gradients to the different layers, as can be obtained from models or from interpolation of nearby occultations or from models. The idea of using neighboring occultations in an iterative fashion in order to improve vertical profile.s was first suggested and now is under investigation by Chiu et al. [29]

Of the most striking characteristics of all the reconstructed profiles of Fig. 12 is that the data are sensitive to the E layer of the ionosphere. Even when the simplest approach is being used, namely when spherical symmetry is assumed, the point-to-point structure of the 1 : layer is recovered, but the overall level is off. By constraining, the solution to fall within lower and upper bounds at certain heights, the overall level can be improved. The GPS provides a unique system for sensing the E layer of the ionosphere which, under normal conditions, can not be detected from ground data alone.

5. CONCLUSION

The importance of choosing the proper basis to expand a solution has been demonstrated in tile ionospheric tomography literature [10, 33]. When choosing a basis, there are two questions to be answered in order to asses how well the ionosphere can be imaged: First, how well does the basis represents actual structures in the ionosphere? Second, how well can these functions be

decorrelated by a given geometry Of links? One way of answering the former question is by examining the post-fit residuals of the data. The answer to the latter question is possible with the application of singular value decomposition analysis, SVD can be very useful to determine what linear combinations of the basis functions the data can resolve and to what accuracy.

Generally speaking, when tomography is employed to reconstruct the ionosphere, one should always expect insufficient strength in the data to obtain a unique solution. Resolution and accuracy are very much dependent on the model used, the variability of the medium and 011 the data noise.

The work clone in this paper suggests that data from space is not sufficient by itself to produce very accurate profiles of the ionosphere, except when horizontal variability is at a minimum, or varies in a way that allows cancellation of rows. On the other hand, ground data are very restricted in sensing vertical structures. 1 lowever, when ground data are used along with data from space, significant improvements are made to the profile solutions. The wide use of GPS suggests that data from several LEO satellite.s tracking GPS will be available in the near future. These data can be used in conjunction with available ground data either directly or to provide needed apriori profiles. Similarly, ground data Call be used to impose constraints on the horizontal structure which the GPS-LEO is insensitive to. The GPS-LEO data is sensitive to small vertical structures in the ionosphere such as the E layer.

ACKNOWLEDGMENTS

A scaled down version of this work has appeared in the *Proceedings* Of *the ION-GPS 93 Conference*, Institute of Navigation, Salt Lake city, Utah, 1993. The work described here was carried 01][at the Jet Propulsion Laboratory, California Institute of Technology, under contract with the National Aeronautics and Space Administration.

REFERENCES

[1] Bassiri S., G. A. Hajj, Higher-order ionospheric effects on the Global Positioning System observables and means of modeling them, *manuscripta geodaetica*, 18:280-289, 1993.

[2] Austen, J. R., S. J. Franke, C. 11. Liu, Ionospheric imaging using computerized tomography, *Radio Sci.*, 23, ?99-307, 19S8.

[3] Na 11., and 11. Lee, Resolution analysis of tomographyic reconstruction of electron density profiles in the ionosphere, *Int. J. Imaging Syst. Technol.*, 2:209-218, 1990

[4] Raymund '1'. 1)., J. R. Austen, S. J. Franke, C. 11. Liu, J. A. Klobuchar, and J. Stalker, Application of computerized tomography to the investigation of ionospheric structures, *Radio Sci.*, 25:77 1-789, 1990.

[5] Na 11., and 11.1 Lee, Orthogonal decomposition technique for ionospheric tomography, *Int. J. imaging Syst. Technol.*, 3:354-365, 1991.

[6] Yeh K. C. and T. D. Raymund, Limitations of ionospheric imaging by tomography, *Radio Sci.*, 26:1361-1380, 1991

[7] Fremouw 1). J., J. A. Secan, B. M. Howe, Application of stochastic inverse theory to ionospheric tomography, *Radio Sci.*, 27:'721-732, 1992.

[8] Kunitsyn V. E. and E. D. Tereshchenko, Determination of the turbulent spectrum in the ionosphere by a tomographic method, *J. of Atmospheric and Terrestrial Physics*, 54:1275-1282, 1992.

[9] Raymund, T. D., s. E. Pryse, L. Kersley, and J. A. T. 1 leaton, Tomographic reconstruction of the ionospheric electron density with 1 European incoherent scatter radar verification, *Radio Sci.*, 28:81 1-81'/, 1993.

[10] Raymund, T. D., S. J. Franke, and K. C. Yeh, Ionospheric tomography: Its limitations and reconstruction methods, *J. Atmos. Terr. Phys.*, in press, 1994.

[11] Fjeldbo G., A. J. Kliore, and V. R. Eshleman, The neutral atmosphere of Venus as studied with the Mariner V radio occultation experiments, *Astronom.. J., 76:123-140, 1971.*

[12] Tyler G. L., Radio propagation experiments in the outer solar system with Voyager, *Proc. IEEE,* **75:1404-1431,** 1987, and references therein.

[13] Bird M. K., S. W. Asmar, J. P. Brenkle, P. Edenhofer, 0. Funke, M. Patzoid, and }1. Volland, Ulysses radio occultation observations of the Io plasma torus during the Jupiter encounter, *Science,* **257:1531-1535, 1** 992.

[14] Hardy **K. R.,** D.P. Hinson, G.L. Tyler, E.R. Kursinski, Atmospheric profiles from active space-basd radio measurements, *Proc. of the 6th conference on Satellite Meteorology and Oceanography,* The American Meteorological Societ y, Boston, 1992.

[1 5] Hardy K. R., Hajj G. A., Kursinski E. R., Accuracies of atmospheric profiles obtained from GPS occultations, *Proc. of the ION-GPS 93 Conf.*, Institute of Navigation, Salt Lake city, 1993.

[16] Kursinski E. R., G. A. Hajj, K. R. Hardy, Temperature or moisture profiles from radio occultation measurements, in *Proc. of the 8th Symp. on Meteorological Observations and Instrumentation*, pp. J153-J158, The American Meteorological Society, Anaheim, 1993.

[17] Kursinski E.R., G. A. Hajj, K. R. Hardy, Atmospheric profiles from radio occultation measurements of GPS satellites, in *Proc. of the International Soc. for Optical Engineering symp. on Optical Engineering and Photonics in Aerospace Science and Sensing*, paper *no. 1935-13,* international Sot. for Optical Eng., Orlando, 1993.

[18] Yuan 1,.1 /., R. A. Anthes, R. H. Ware, C. Rocken, w. D. Bonner, h4. G. Bevis, S. Businger, Sensing climate change using the Global Positioning System, *J. of Geophys. Res.* 98:14925-14937, 1993.

[19] Spilker J. J., GPS signal structure and performance characteristics, *Navigation,* 25:29-54, 1978.

[20] Wilson B. D. and A. J. Mannucci, Instrumental biases in ionospheric measurements derived from GPS data, *Proc. of the ION-GPS 93 Conf.*, Institute of Navigation, Salt Lake city, 1993.

[21] Blewitt G., M. B. Heflin, K. J. Hurst, D. C. Jefferson, F. H. Webb, J. F. Zumberge, Absolute far-field displacements from the 28 June 1992 Landers earthquake sequence, *Nature*, 361:340-342, 1993.

[22] Freedman A. P., Measuring earth orientation with Slobs] positioning system, *Bull. Geod.* 65:53-65, 1991.

[23] Malla R. P., S.C. Wu, S. M. Lichten, Geocenter location and variations in earth orientation using global positioning system measurements, J. *of Geophys. Res.* **98:4611-461 'i, 1993**

[24] Bertiger W. I., J.T. Wu, S.C Wu, Gravity field improvement using GPS data from Topex/Poseidon: a covariance analysis, *J. of Geophys. Res. 97:1965-* **1971, 1992.**

[25] Tralli D. M., S. M. Lichten, Comparison of Kalman filter estimates of zenith atmospheric path delays using the Global Positioning System and very long base-line interferometry, *Radio Sci.*, **27:999-1007, 1992.**

[26] Wilson B. D., A. J. Mannucci and P. Roth, Global ionospheric maps using a global network of GPS receivers, *Proc. of the International Beacon Satellite Symposium, cd* ited by M.C. Lee, pp. ***144-147,*** Plasma Fusion Center, Massachusetts Institute of Technology, Beacon Satellite Symposium, 1992.

[27] Coco D, GPS-Satellites of opportunity for ionospheric monitoring, *GPS World*, Oct, pp 47-50, 1991.

[28] Yunck P. P., G.F. Lindal, C.H. Liu, The role of GPS in precise earth observation, *Proc. of IEEE position location and navigation symposium,* Orlando, 1988.

[29] Chiu, Y. P., R. M. Robinson, and G. P. Davidson, Global **3-d** monitoring of the ionosphere with space-based GPS receivers, in *Proc. of the International Beacon Satellite*

Symposium, M.C. Lee, ed., pp. 148-151, Plasma Fusion Center, Massachusetts Institute of Technology, Beacon Satellite symposium, 1992.

[30] Mannucci J. A., B.D. Wilson, C. D. Edwards, A new method for monitoring, the earth's ionospheric total electron content using the GPS global network, Proc. of the *ION-GPS 93 Conf.*, Institute of Navigation, Salt Lake city, 1993.

[31] Wilson, B. D., A. J. Mannucci, C. D. Edwards, Sub-daily northern hemisphere ionospheric maps using the IGS GPS network, *Proc. of the 7th International Ionospheric Effects Symp.*, J. Goodman, ed., Alexandria, VA, 1993.

[32] Wiggins R. A., The general linear inverse problem: implication of surface waves and free oscillations for earth structure, Rev. *of Geophy. and Space Phys.*, 10:251-285, 1972,

[33] Raymund T. D., *Development and Applications of Ionospheric Tomography*, Ph.D. Thesis, University of Illinois at Urbana-Champaign, Urbana, IL, 1993.

[34] Na H., *Tomographic Reconstruction Techniques for Imaging Electron Density Profiles in the Ionosphere*, Ph.D. thesis, University of Illinois at Urbana-Champaign, Urbana, IL, 1991.

FIGURE CAPTIONS

Figure 1: Occultation geometry for GPS and a low earth orbit satellite,

Figure 2: The Global Positioning System configuration

Figure 3: Viewing geometry (off scale), Dividing the ionosphere into 20x20 pixels.

Figure 4: Singular Values of the example of Fig. 3.

Figure 5: The reconstruction of a unit impulse function at pixel *270,* including 100" singular values

Figure 6: Resolution and the corresponding error in the neighborhood of pixel *270* for different numbers Of SV's included in the solution.

Figure 7: A finite and discrete 2-D image of the ionosphere illustrating the dependence of the data strength on the basis functions.

Figure 8: Simulated electron density using the PIM model at 20 GE geodetic longitude, at 12:00 111.11'1'.

Figure 9: Tomographic reconstruction of the *2-1)* image of Fig. 7, with 7 ground stations at -20°, *-1* 0°, 0°, 10°, 20°, 30° and 40° north longitude. (a) No occultation data included; (b) including occultation data.

Figure 10: A representative daily occultation coverage for GPS-MET (total of 219 occultations).

Figure 11: Delay and bending of the GPS L1 signal as it travels the. earth's ionosphere.

Figure 12: Vertical slices of the 2-D image of Fig. 8 at (a) -20° *N;* (b) 0° *N;* (c) 20° *N;* (d) 40° N. Showing truth (solid line) versus reconstructed assuming spherical symmetry (open diamond), and reconstructed assuming some horizontal gradient (solid square).

Figure 13: Indexing convention of pixels in polar coordinates.

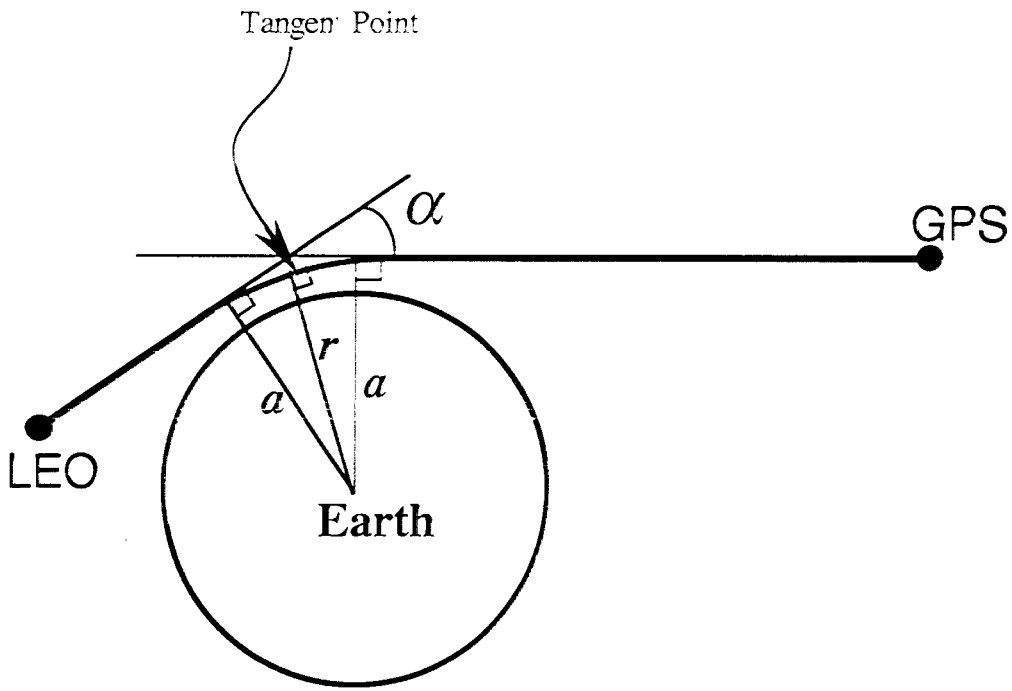

Fig 1

Fig 2

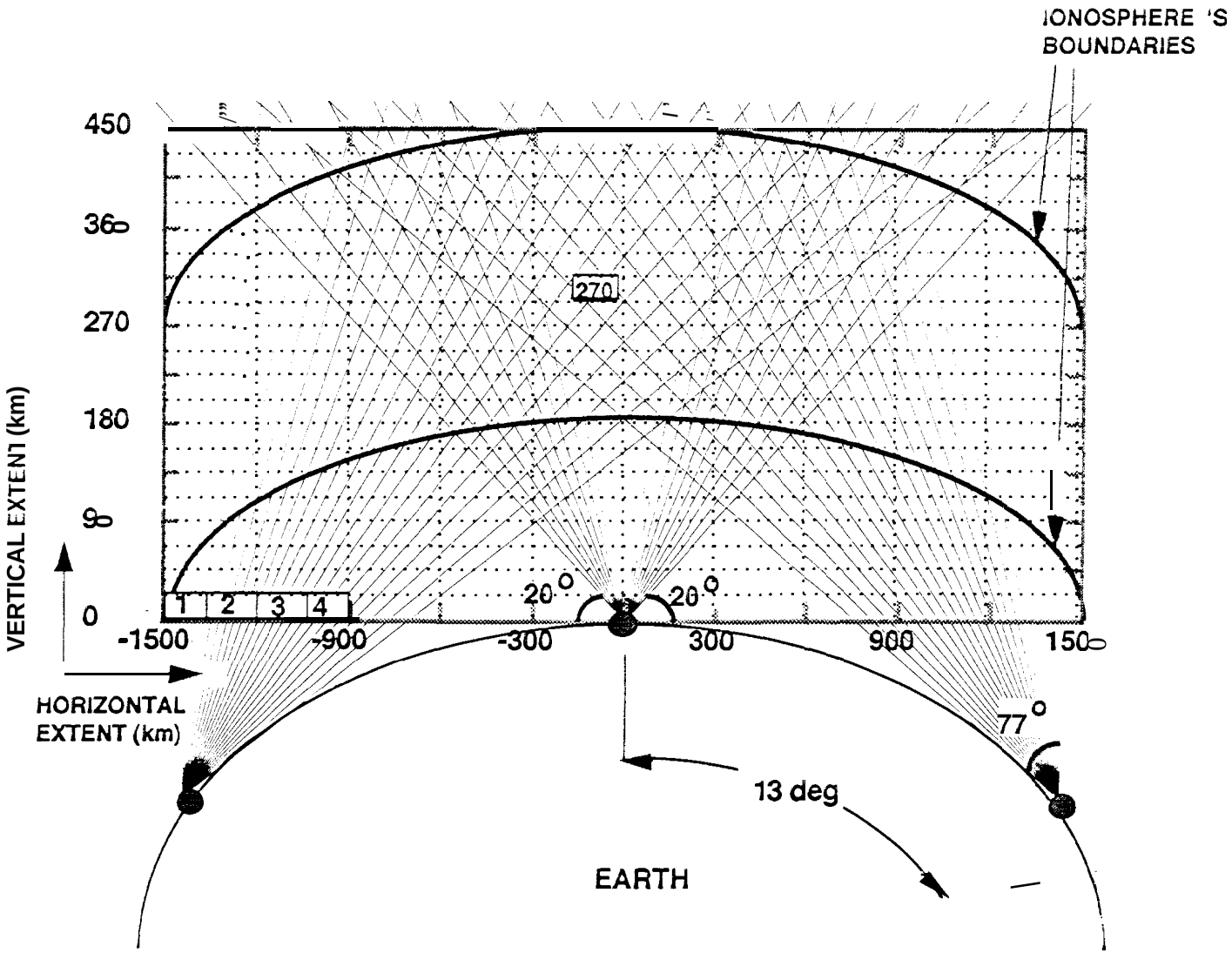
IONOSPHERE 'S
BOUNDARIES
450
360
270
180
90
0
VERTICAL EXTENT (km)
270
1
2
3
4
20°
20°
-1500
-900
-300
300
900
1500
HORIZONTAL
EXTENT (km)
77°
13 deg
EARTH

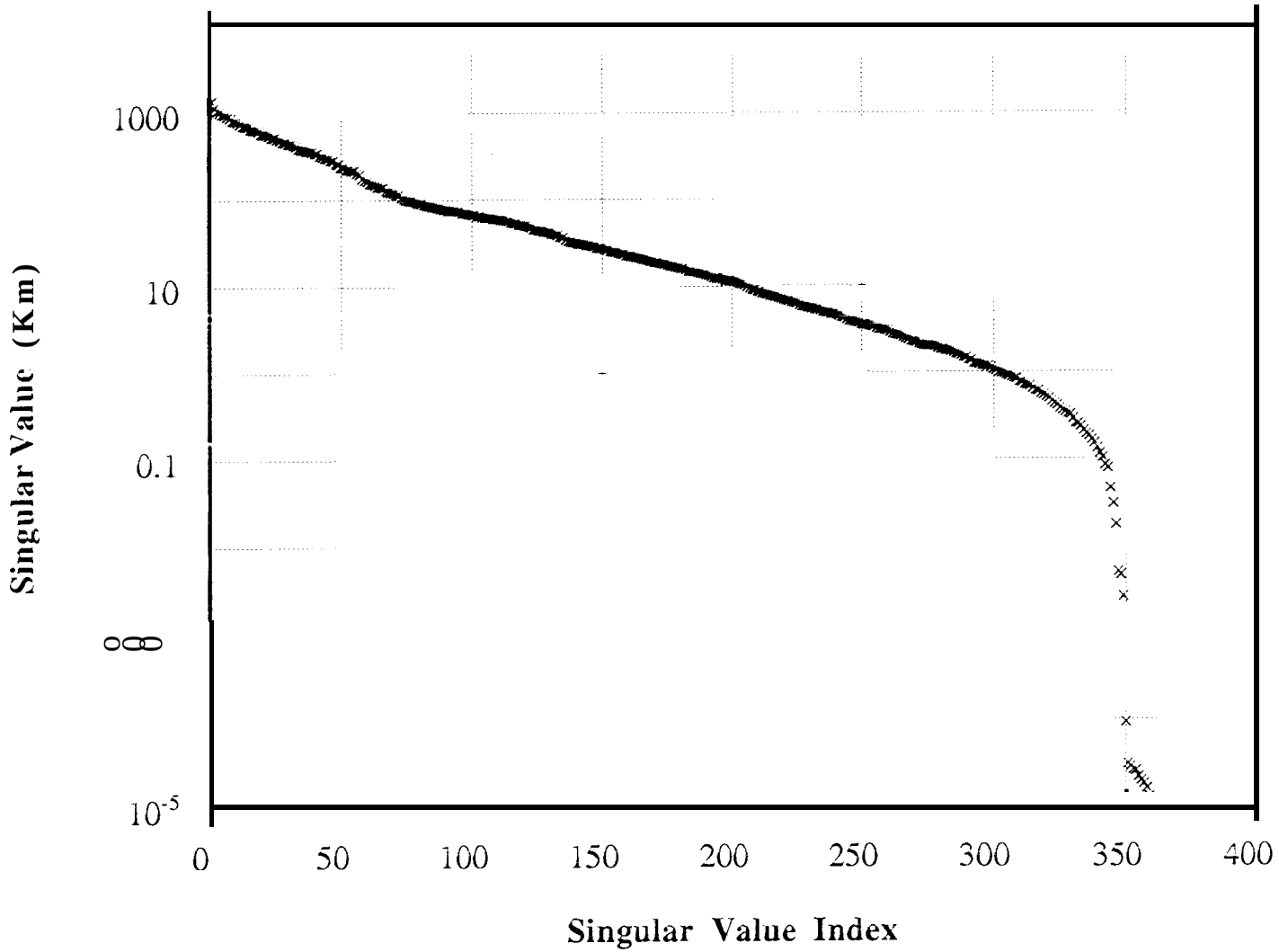
1000
10
0.1
10^{-5}
0
50
100
150
200
250
300
350
400
Singular Value (Km)
Singular Value Index

Fig. 4

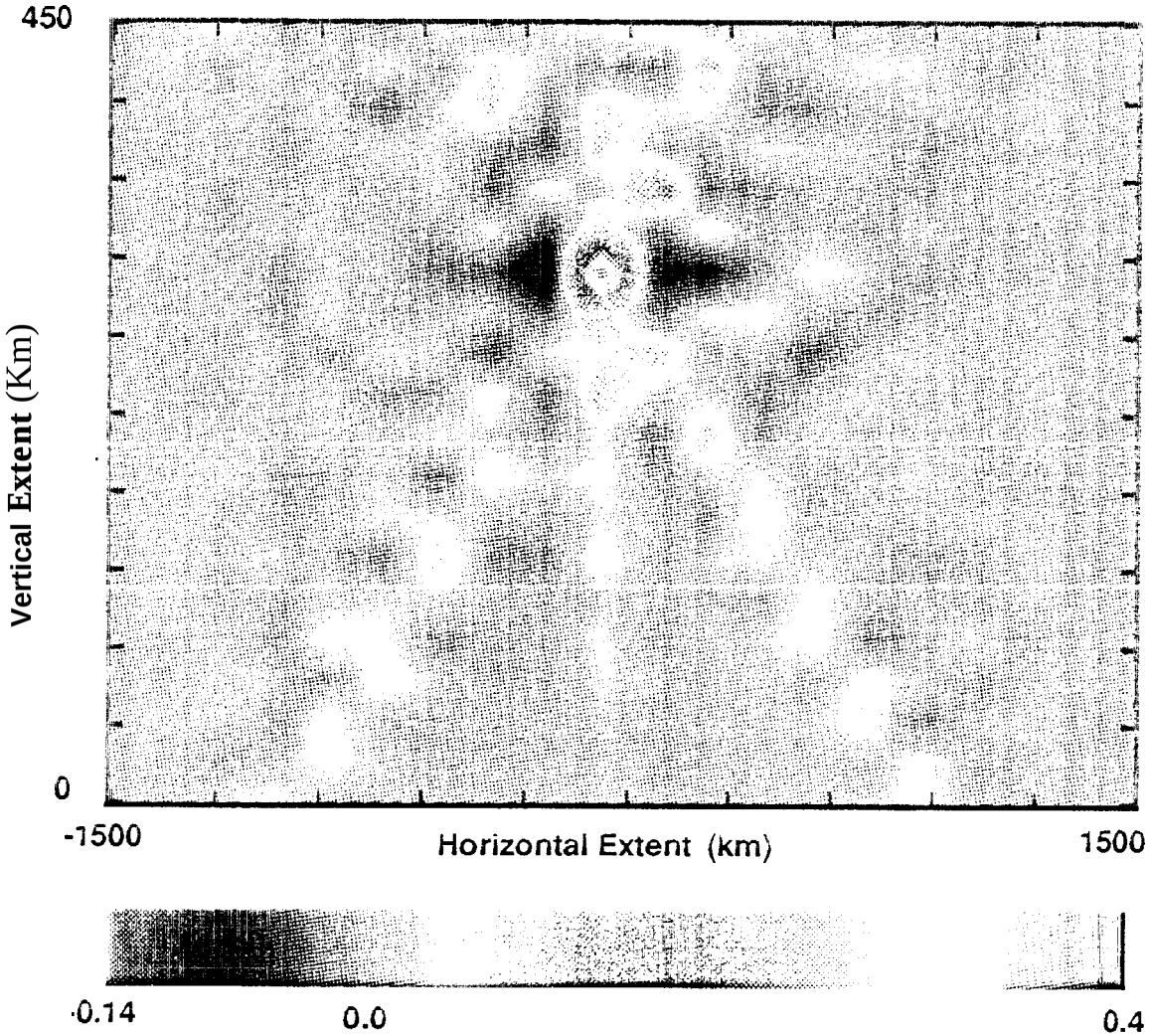
450
0
Vertical Extent (Km)
-1500
Horizontal Extent (km)
1500
-0.14
0.0
0.4

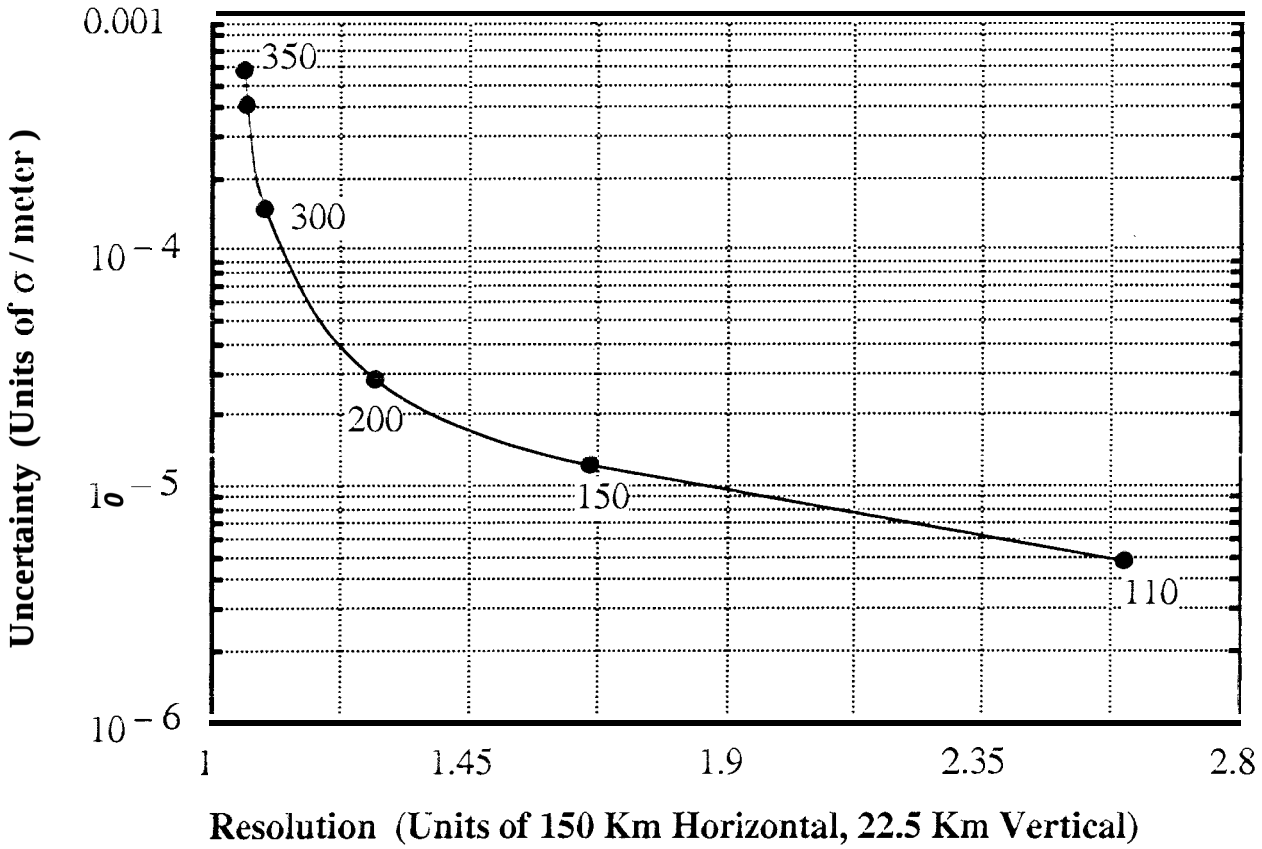
0.001
10^{-4}
10^{-5}
10^{-6}
Uncertainty (Units of σ / meter)
350
300
200
150
110
1
1.45
1.9
2.35
2.8
Resolution (Units of 150 Km Horizontal, 22.5 Km Vertical)

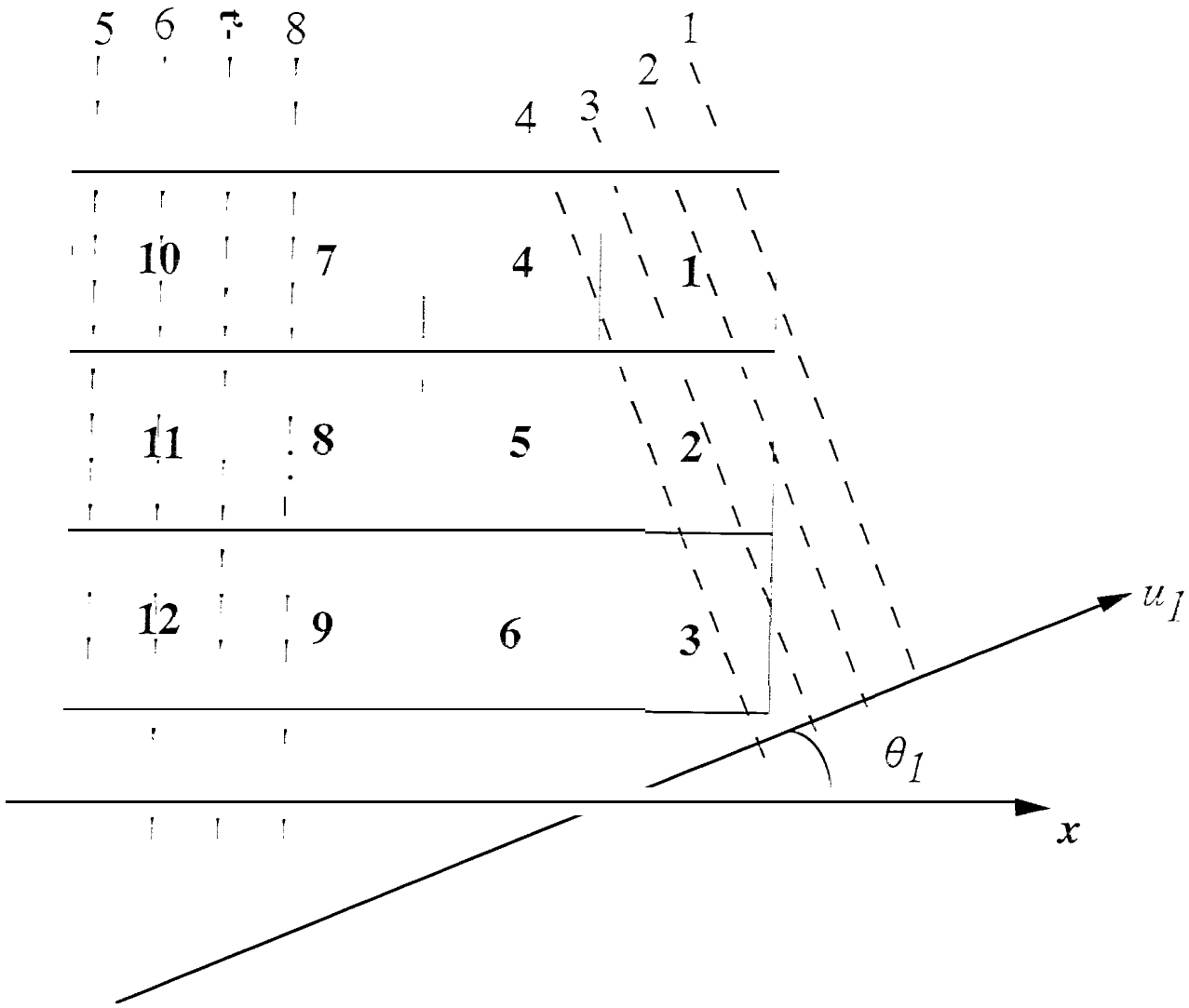

figure 7

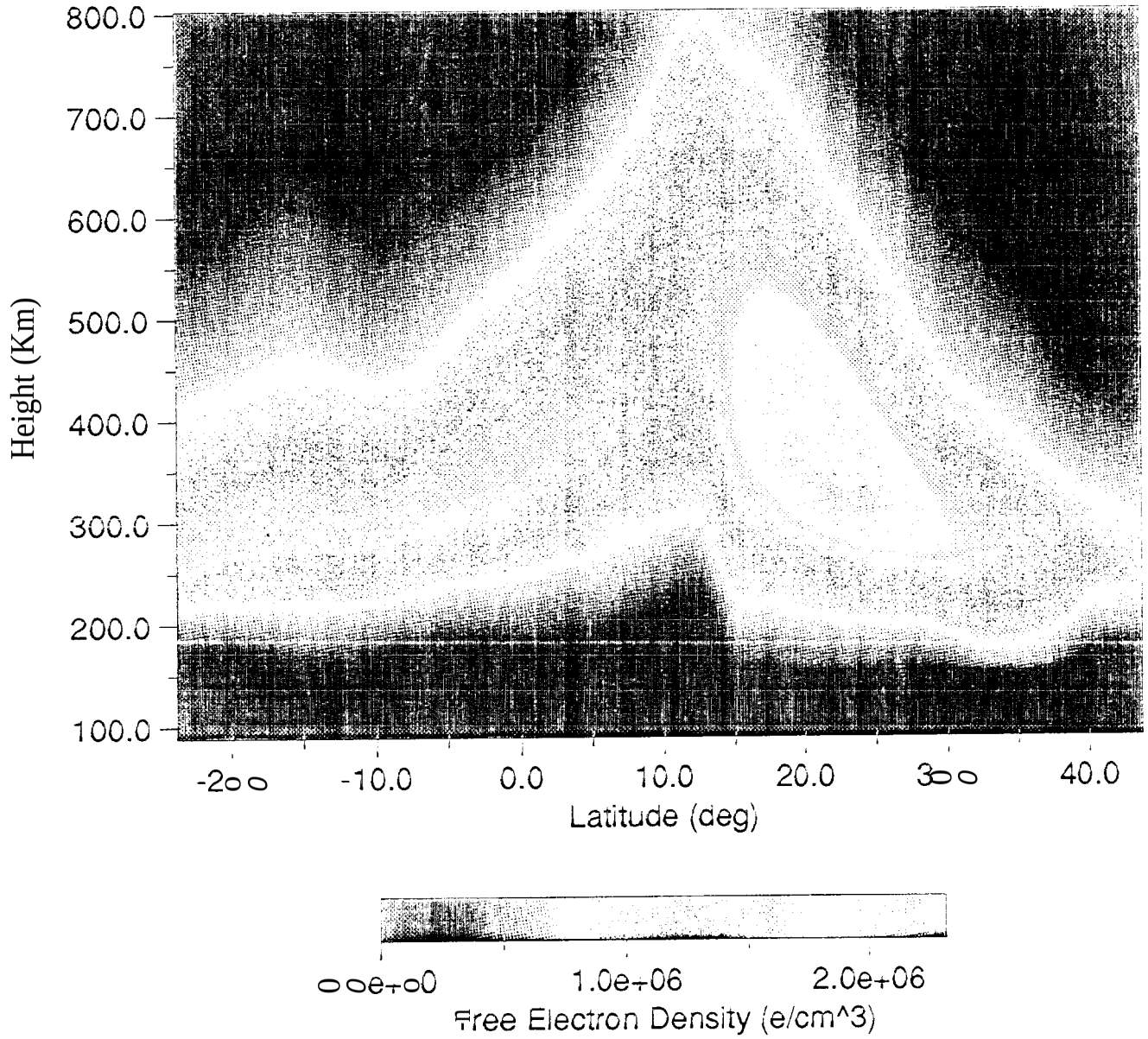
800.0
700.0
600.0
500.0
400.0
300.0
200.0
100.0
Height (Km)
-20.0
-10.0
0.0
10.0
20.0
30.0
40.0
Latitude (deg)
0.0e+00
1.0e+06
2.0e+06
Free Electron Density (e/cm^3)

Fig 8

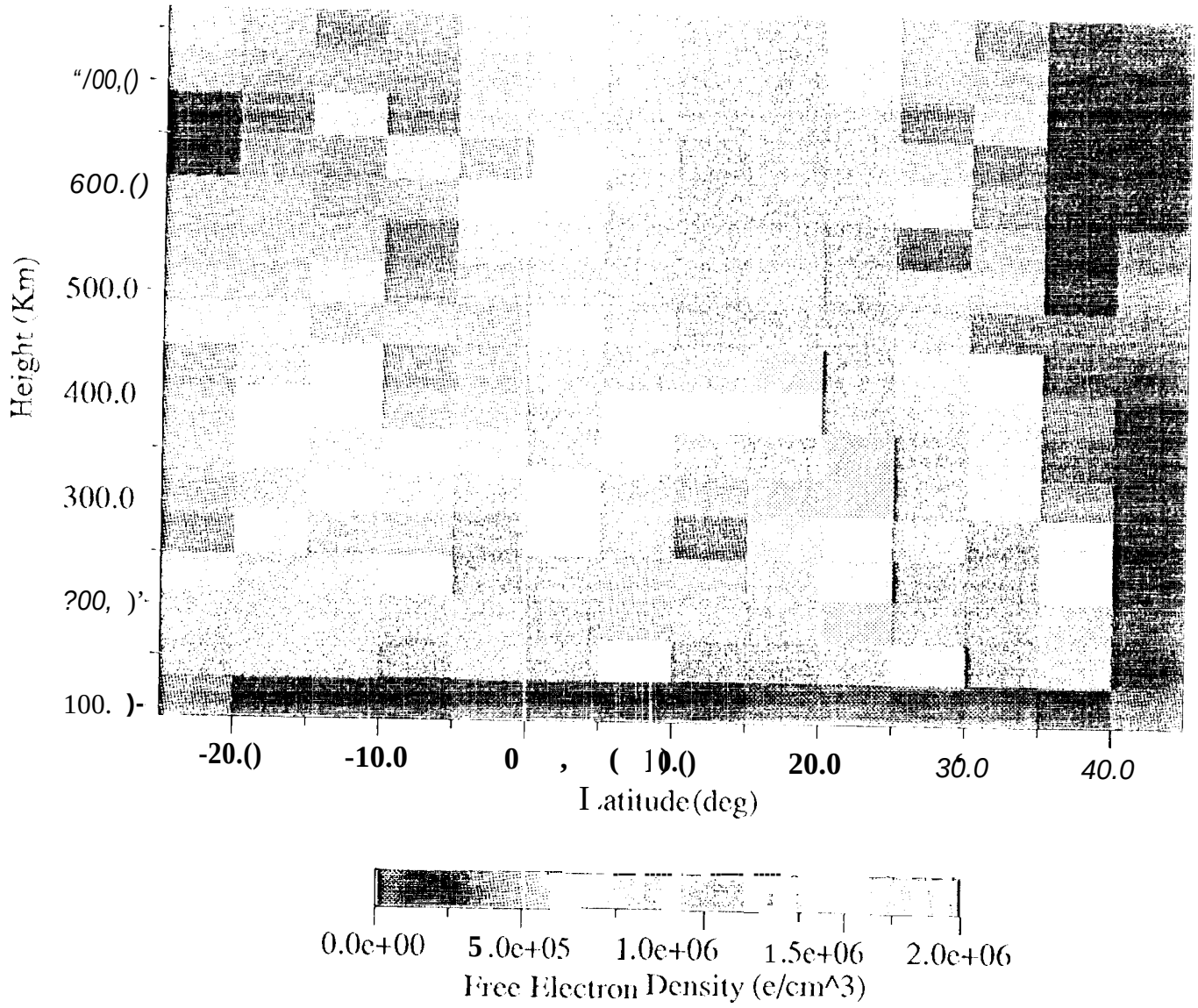
"/00,()
600.()
500.0
400.0
300.0
?00,)'
100.)-
Height (Km)
-20.()
-10.0
0
10.()
20.0
30.0
40.0
Latitude (deg)
0.0e+00
5.0e+05
1.0e+06
1.5e+06
2.0e+06
Free Electron Density (e/cm^3)

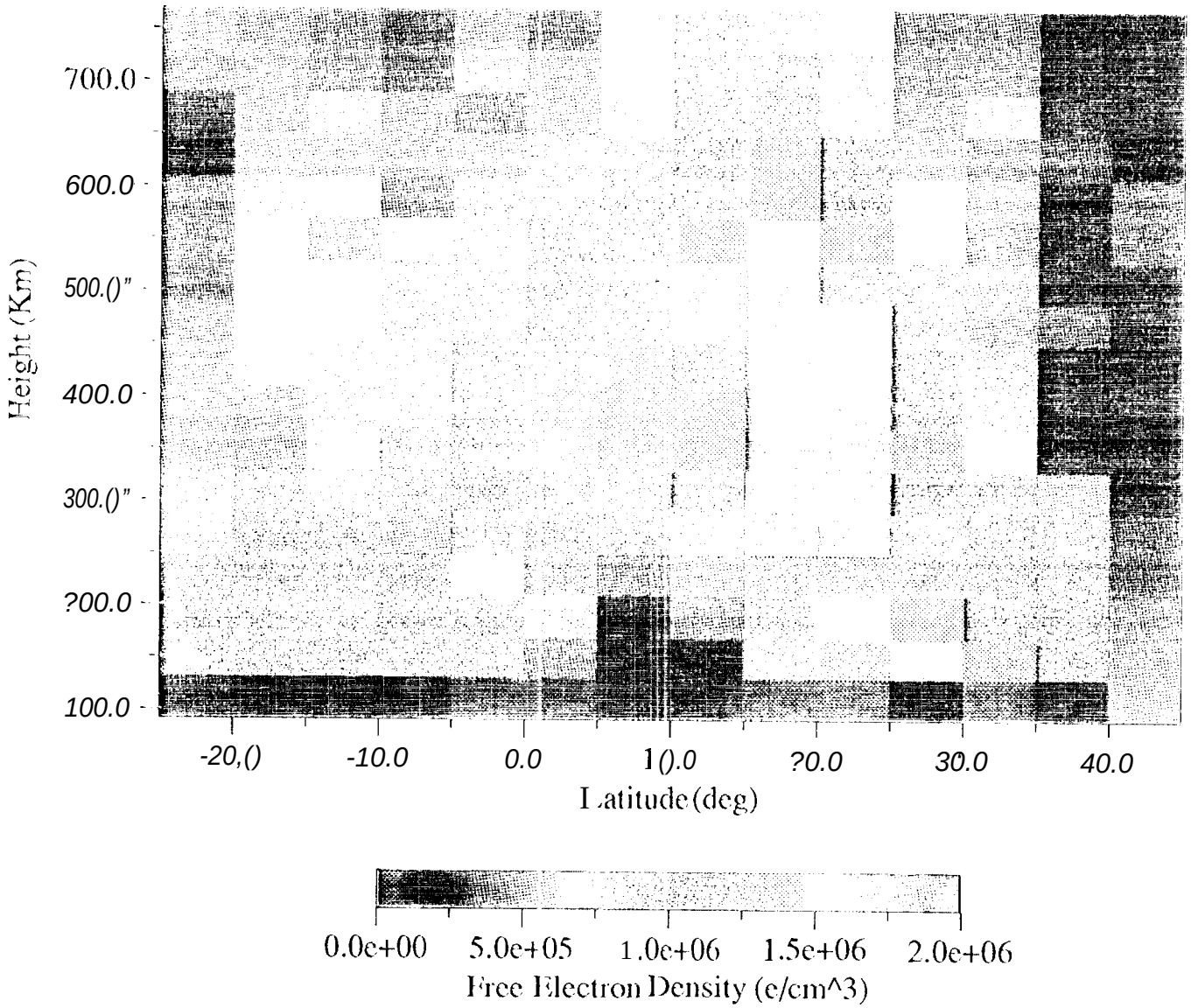
700.0
600.0
500.()"
400.0
300.()"
?00.0
100.0
Height (Km)
-20,()
-10.0
0.0
1().0
?0.0
30.0
40.0
Latitude (deg)
0.0e+00
5.0e+05
1.0e+06
1.5e+06
2.0e+06
Free Electron Density (e/cm^3)

fig 9.b

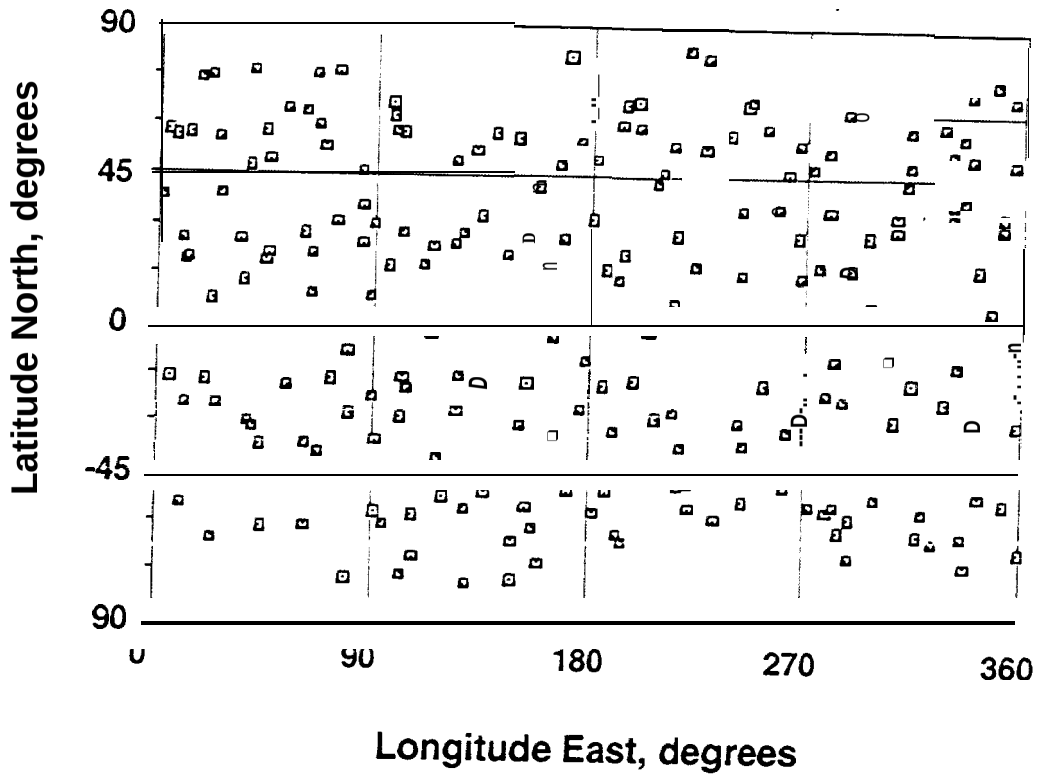
90
45
0
-45
90
0
90
180
270
360
Latitude North, degrees
Longitude East, degrees

figure 10

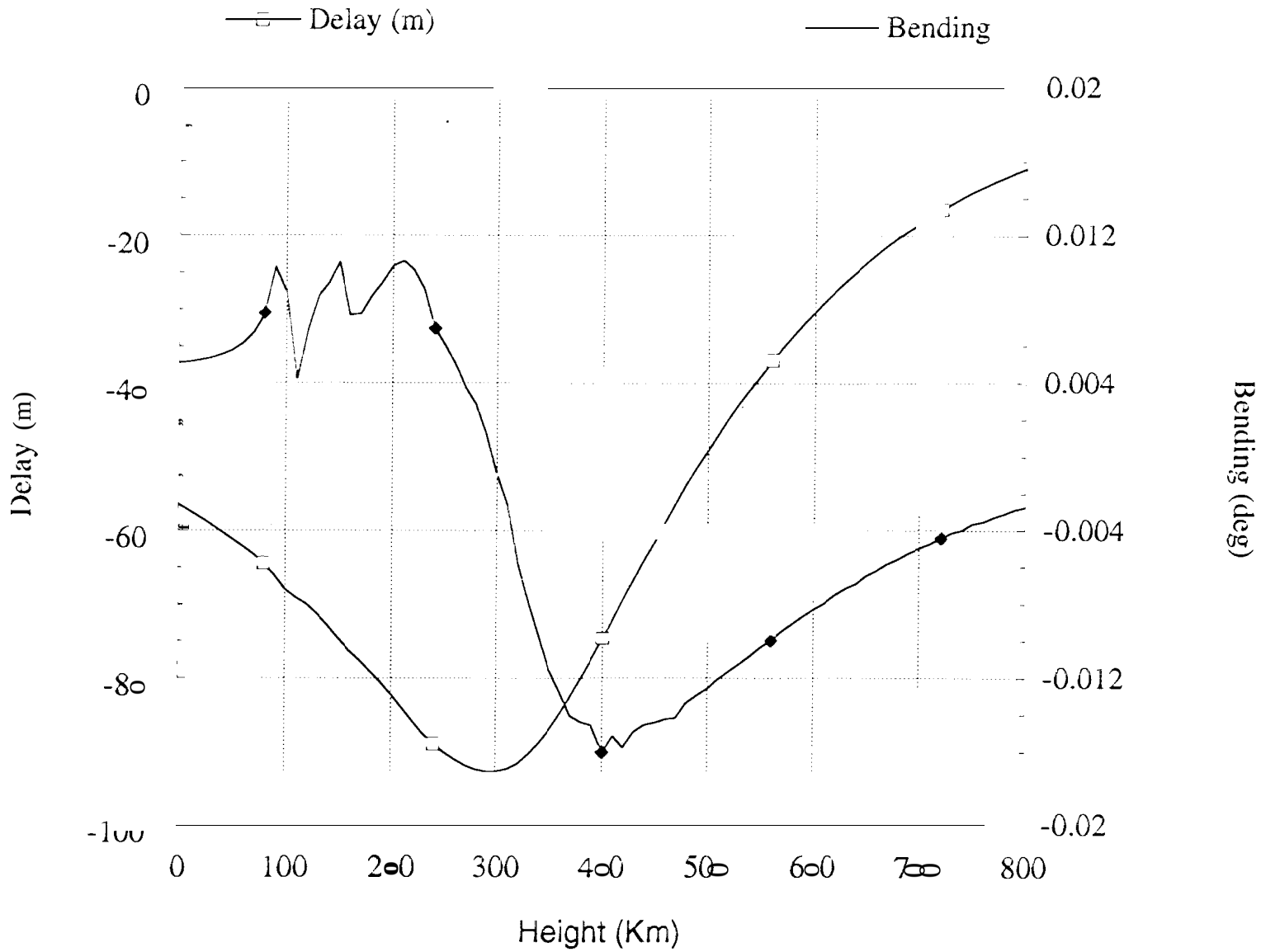
Delay (m)
Bending
0
-20
-40
-60
-80
-100
0.02
0.012
0.004
-0.004
-0.012
-0.02
0
100
200
300
400
500
600
700
800
Height (Km)
Delay (m)
Bending (deg)

figure 1

figure 12.a

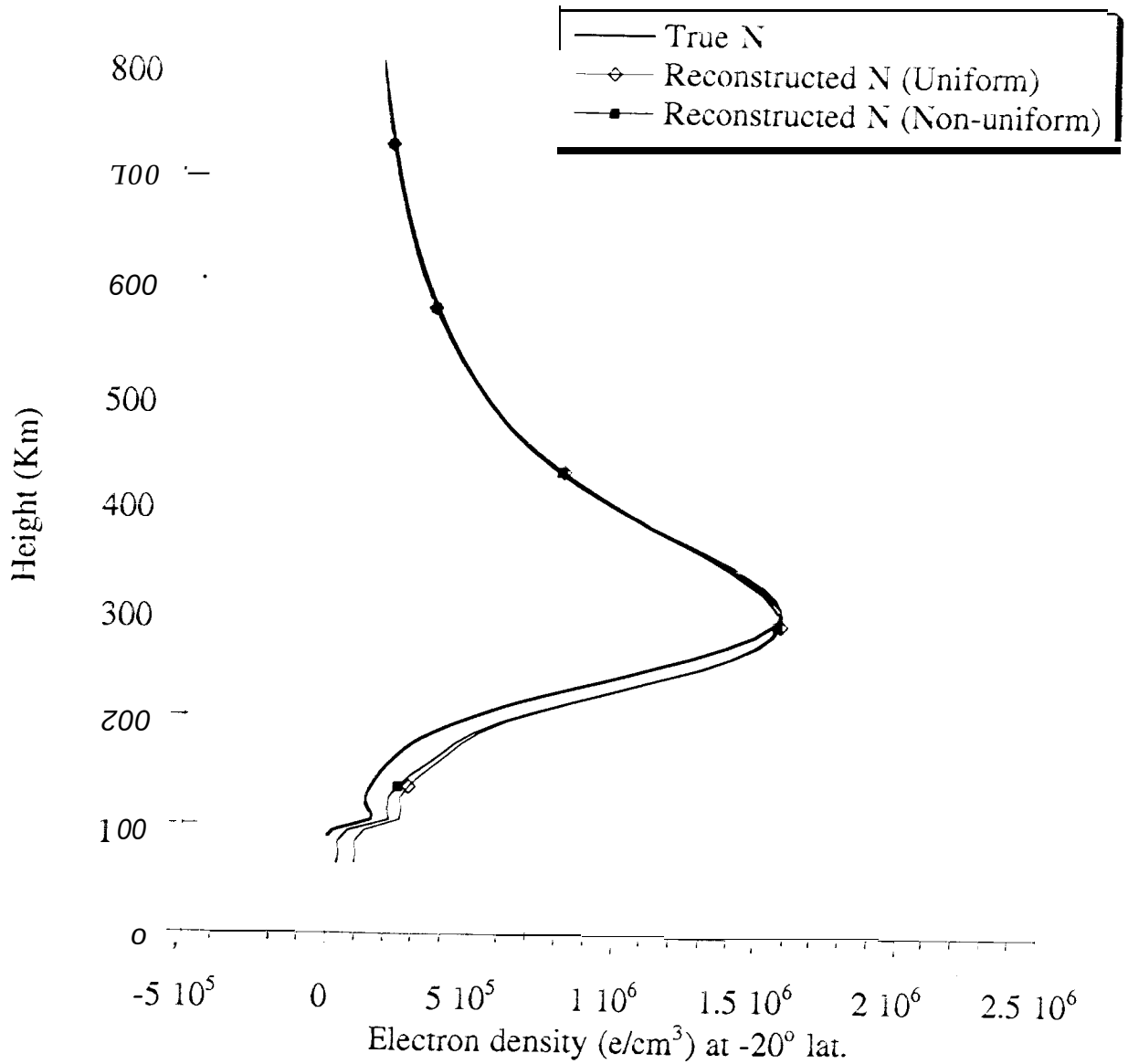
True N
Reconstructed N (Uniform)
Reconstructed N (Non-uniform)
Height (Km)
800
700
600
500
400
300
200
100
0
-5 10^5
0
5 10^5
1 10^6
1.5 10^6
2 10^6
2.5 10^6
Electron density (e/cm^3) at -20° lat.

(a)

figure 12 b

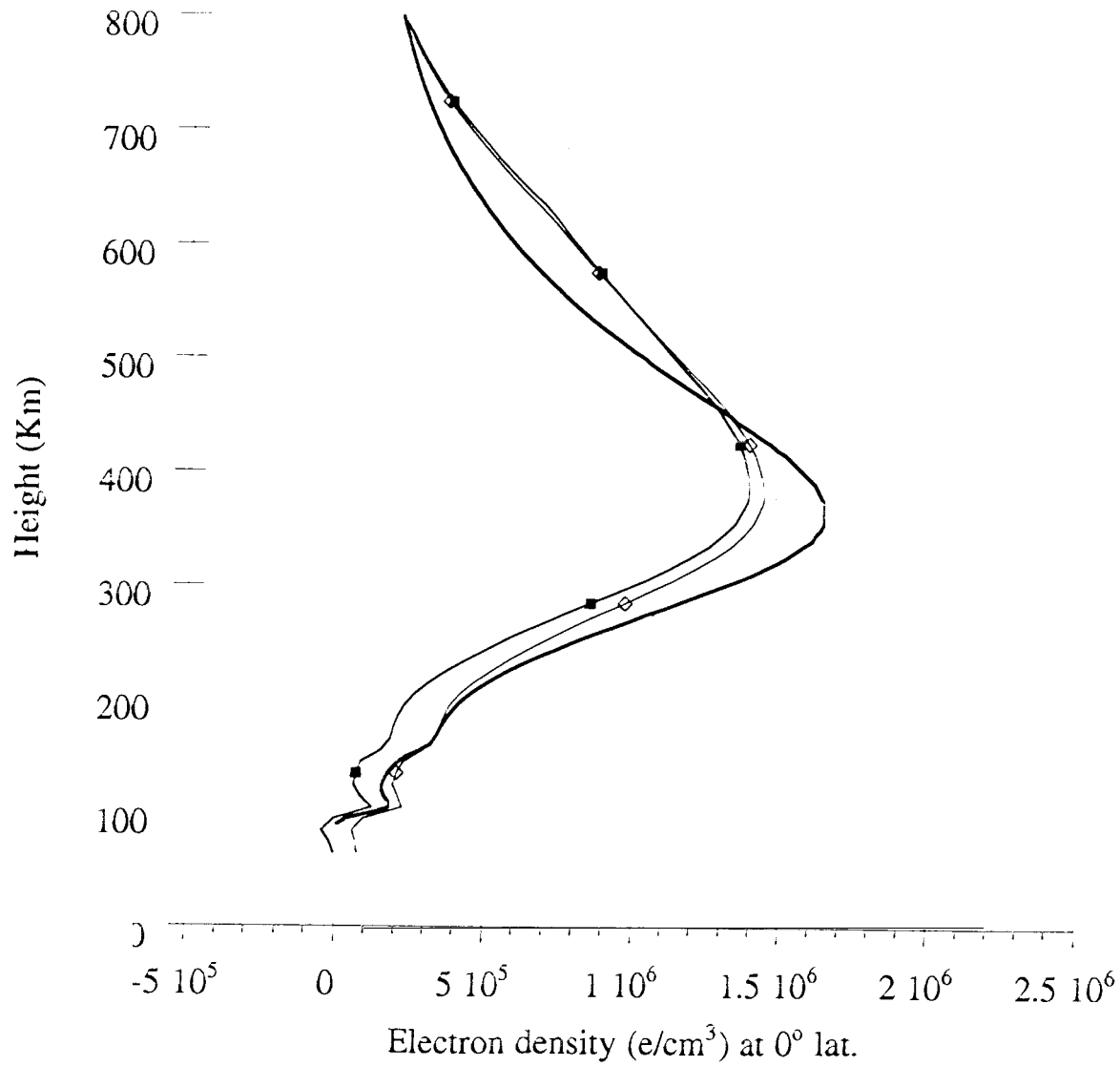
800
700
600
500
400
300
200
100
0
Height (Km)
-5 10^5
0
5 10^5
1 10^6
1.5 10^6
2 10^6
2.5 10^6
Electron density (e/cm^3) at 0° lat.

(b)

figure 12.c

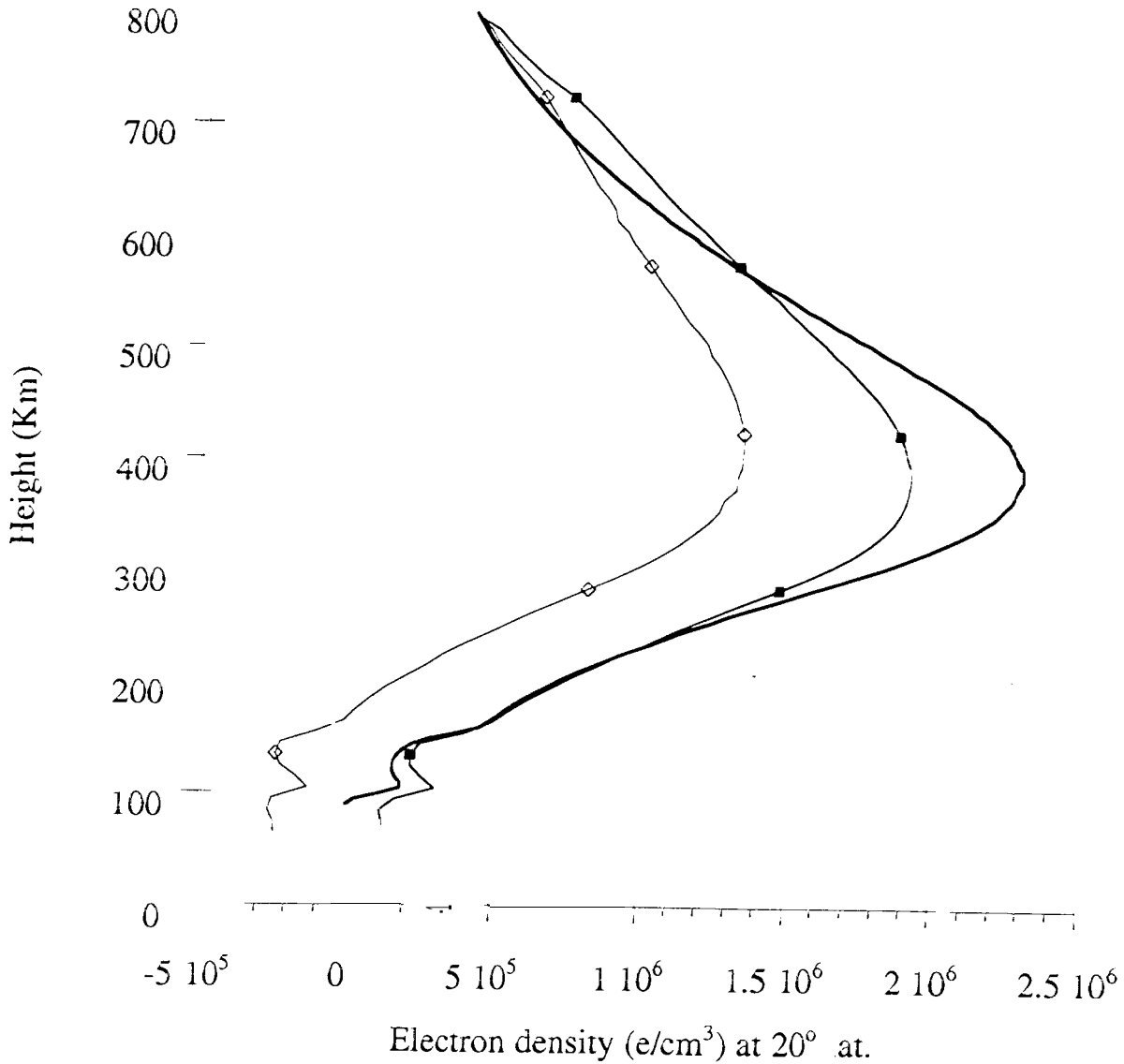
800
700
600
500
400
300
200
100
0
Height (Km)
-5 10^5
0
5 10^5
1 10^6
1.5 10^6
2 10^6
2.5 10^6
Electron density (e/cm^3) at 20° at.

(c)

figure 12.d

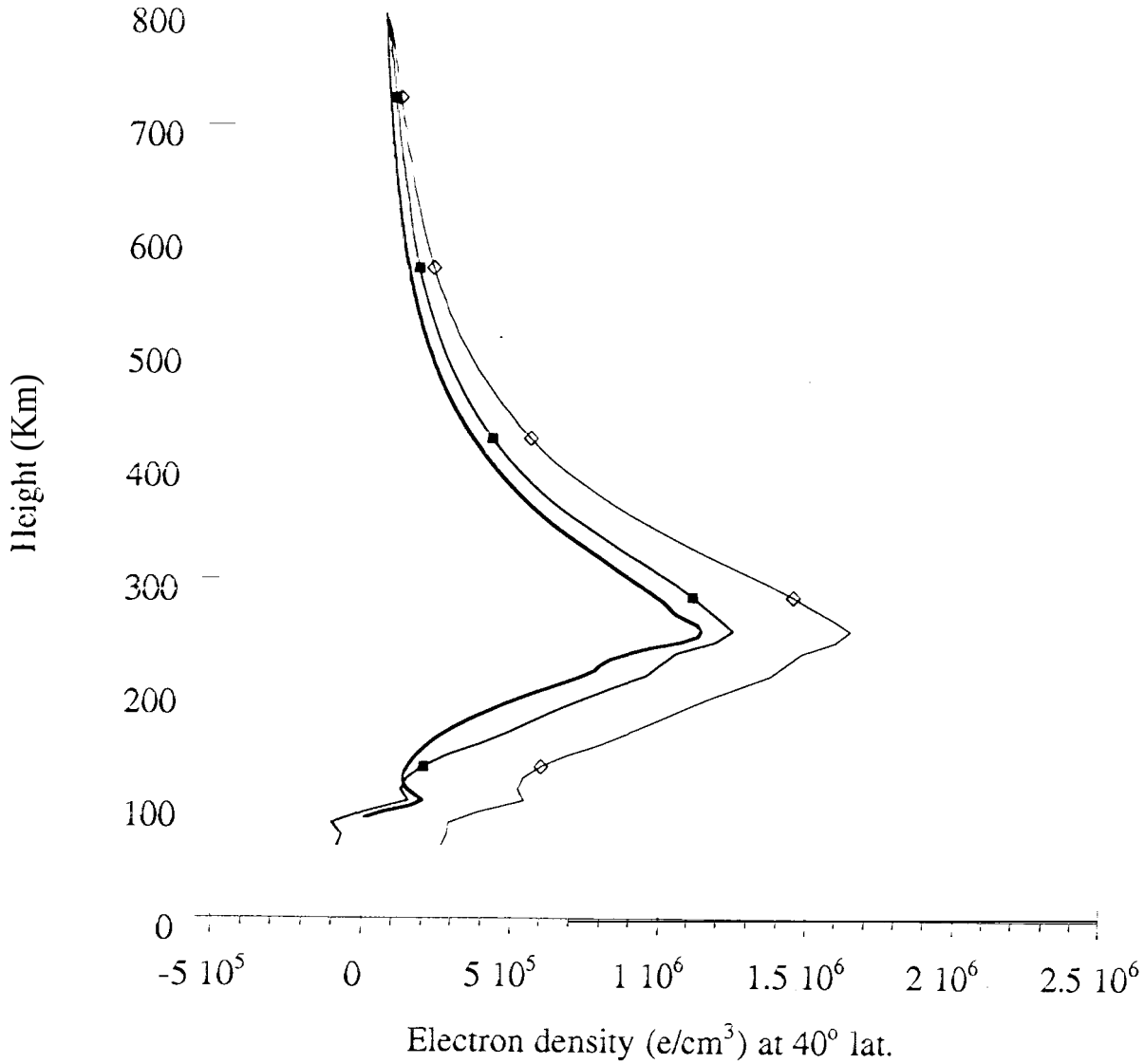
800
700
600
500
400
300
200
100
0
Height (Km)
-5 10^5
0
5 10^5
1 10^6
1.5 10^6
2 10^6
2.5 10^6
Electron density (e/cm^3) at 40° lat.

(d)

Figure 13

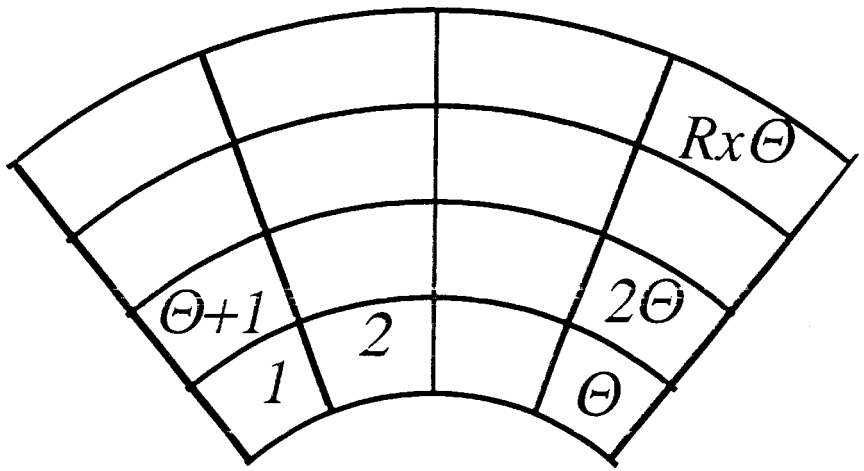
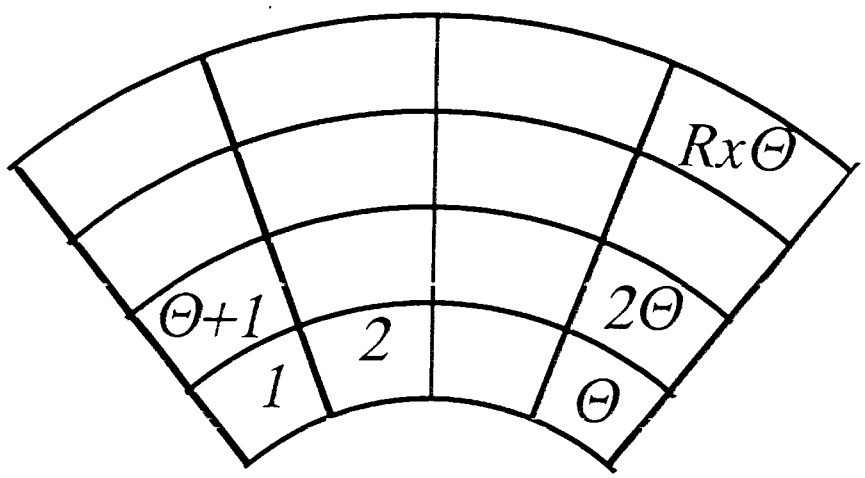
Figure 13